J Therm Anal Calorim (2015) 119:1323–1338
DOI 10.1007/s10973-014-4217-1

Simulation, aggregation and thermal analysis of nanostructured calcite obtained in a controlled multiphase process

Małgorzata Wszelaka-Rylik · Katarzyna Piotrowska · Paweł Gierycz

Received: 16 May 2014 / Accepted: 27 September 2014 / Published online: 31 October 2014

Abstract In the present experiments, the carbonation process in multiphase system was carried out using the reactor with rotating discs. Calcite was produced by controlled fast precipitation through gaseous CO_2 adsorption in $Ca(OH)_2$ slurry. Furthermore, the reaction kinetics' were controlled by disc's revolution speed in the range from 80 rpm through 120 to 160 rpm. Initial concentration of the slurry ranged between 54 and 110 mM L^{-1}. The aggregates of crystals precipitated in the aqueous solution were of sub-micrometric size. Dynamic light scattering method showed that mean aggregate diameter decreased with the higher mixing rate as long as the mixing condition was homogenous (up to 160 rpm). Thermogravimetric analysis revealed that the surface of calcite was polluted by unwanted, different compounds amount of which depends on the initial concentration of the slurry. Therefore, in order to obtain chemically pure calcite, $CaCO_3$ powder was heated up in the laboratory oven. In order to explain the mechanism of calcite particles' aggregation, the simulation of the aggregates formation has been performed based on the new model taking into account kinetics of the multiphase reaction, crystal growth and their agglomeration. The obtained data on crystal morphology during the precipitation process have been compared with the model simulation results. The internally consistent model very well describes both the formation and the aggregation of the calcite nanoparticles, and the same can be used and recommended for accurate calculations of the particle and aggregates' sizes as well as their distribution in the reactor.

Keywords Nanostructured material · Thermal analysis · Computer simulation · Gas–liquid precipitation · Calcium compounds

M. Wszelaka-Rylik
Faculty of Biology and Environmental Sciences, Cardinal Stefan Wyszynski University in Warsaw, Wóycickiego 1/3, 01-938 Warsaw, Poland

K. Piotrowska
Institute of Physical Chemistry of Polish Academy of Science, Kasprzaka44/52, 01-224 Warsaw, Poland

P. Gierycz (✉)
Faculty of Chemical and Process Engineering, Warsaw University of Technology, Warynskiego 1, 00-645 Warsaw, Poland
e-mail: p.gierycz@ichip.pw.edu.pl

Introduction

Calcium carbonate is one of the most widely used fillers in many industrial applications such as plastics, rubber, paper making and medicine. Furthermore, the nanocrystalline calcium carbonate has many more advantages compared to the commonly used normal size calcium carbonate, and for this reason, it has been attracting wide research interests [1]. Therefore, development of "smart," cheap and energy-saving method, which allows one to obtain nanocrystallites of calcium carbonate, is in great demand in industry. However, despite a large number of investigations described in the literature [2–17], the mechanisms of the molecular level of calcium carbonate precipitation as well as the aggregation and formation processes [2–7, 9–14] are still unclear and have not so far been fully understood. It concerns also the classical nucleation pathway of calcium carbonate precipitation, i.e. formation of a critical nucleus, followed by stepwise growth of the crystal [18]. In general, there are two established mechanisms of crystal growth described in the literature [2, 15]. Ostwald ripening involves the formation of larger crystals from smaller

crystals that have higher solubility than larger ones do. So, the smaller crystals act as fuel for the growth of the larger crystals. Another important growth mechanism revealed in recent years is non-classical crystallization mechanism by aggregation, i.e. coalescence of initially stabilized nanocrystals that grow together and form one larger particle [15, 19]. Several studies have demonstrated that the incorporation and sorption of inorganic/organic impurities inhibit the crystal growth process of calcite [20–23]. Conversely, the nucleation process may be enhanced, leading to a complex aggregation/agglomeration process of small particles, resulting in clusters of crystallites, as observed in the present study.

The main objective of this work is to characterize calcium carbonate aggregates of nanoparticles obtained in a controlled multiphase system by use of the reactor with rotating discs (RDR) [24, 25]. The multiphase formation of $CaCO_3$ is important not only from the theoretical point of view, but also from that of fundamental applicative implications in the field of cultural heritage conservation. Demineralization processes that are strongly dependent on the way of formation and the aggregation of $CaCO_3$ nanocrystals affect several kinds of artefacts, such as carbonatic stones [26] or archaeological and palaeontological bones [27].

The single size of nanoparticles formed in the reactor used is equal to ca. 30 nm [24, 25], but the size of their aggregates depends strongly on the reaction conditions. Because aggregates of $CaCO_3$ nanoparticles covered by organic substances find nowadays wide industrial applications (pharmaceuticals, synthetic bone, semi-permeable membranes, etc. [28–30]), the aim of the current study was to find solutions concerning possibilities in the production of ultrafine, well-defined (depending on the process conditions) calcite powder aggregates, in the rotating disc reactor without any additives. From our previous studies [24, 25], we know that the nanostructured $CaCO_3$ powder is very pure, thermodynamically stable and has well-developed specific surface area [24]. In this study, we intended to check whether the aggregation process of nanoparticle can be controlled by mixing conditions in the rotating disc precipitation reactor and the initial calcium hydroxide suspension content.

To better explain the mechanism of nanoparticles agglomeration in the reactor, we extended our previous precipitation reaction model [25] and applied it for the simulation of aggregates' formation during the reaction in the rotating disc precipitation reactor. The model has taken into account not only kinetics of the multiphase reaction and crystal growth rate but also nanoparticles' agglomeration. The data obtained, during the precipitation process, concerning aggregates' formation were compared to the simulation results of the model.

Experimental

Materials and solutions

Carbon dioxide used in the experiments was taken directly from a gas bottle (99.9993 % pure, from Linde) and calcium hydroxide from a pure sample (p.a. from POCH Gliwice Poland). The chemicals were used without any further purification.

All samples were prepared using double-distilled and deionized water. Three differential initial concentrations of calcium hydroxide were used for the experiments: 23, 54 and 110 mM. The slurries were prepared by dispersing, respectively, 1.7, 4 or 8 g of $Ca(OH)_2$ powder into 100 mL of deionized water, in a volumetric flask. Next day, the slurries were treated in an ultrasonic bath for 10 min, then the solution was cooled down to 25 °C, diluted to make up a volume of 1 l and immediately used for experiments.

Precipitation procedures

In the present experiments, the carbonation process was carried out in multiphase system using the RDR [24, 25], as shown in Fig. 1. The one-reactor chamber that was used in the experiments has a maximum volume of liquid reactant equal to 2 l. Before each experiment, the reactor elements were cleaned with 10 % HCl solution to get rid of any $CaCO_3$ particles and then rinsed with deionized water. All processes were performed under atmospheric pressure and at the constant temperature of the solution equal to 25 °C. The rate of gas inflow to the reactor was equal to 2 l min^{-1} and was maintained at a constant level by Mass Flow Controller GFC (Aalborg) calibrated using CO_2.

The reaction kinetics were controlled by disc's revolution speed ranging from 80 revolutions per minute (rpm) through 120 rpm, and then up to 160 rpm. The carbonation process was stopped when the whole solution became neutralized (pH 7). Then, the precipitated solids were collected by filtering through membrane filter (0.1μm), dried in 80 °C for 24 h, and finally stored in a desiccator. The liquid-phase volume was equal to 1 l, and the interface area was equal to 0.142 m^2.

Characterization techniques

The pH changes during reaction were measured by means of combined glass electrode (IJ-44 for sewage and ultrapure water, IONODE, Australia). The pH meter was coupled with PC, and the experimental data were collected every second for the adjustment of carbonation time. Electrode was calibrated before every experiment using three buffer solutions (CHEMPUR, Poland; pH values at 25 °C were equal to 7.0, 9.0, and 12.0, respectively).

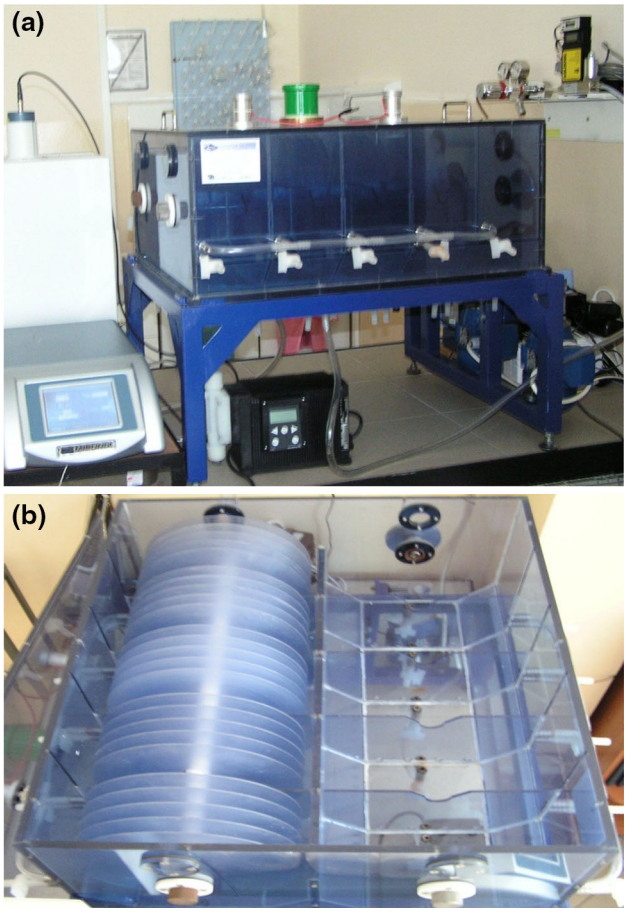

Fig. 1 The rotating disc reactor system: **a** general view, **b** reactor chamber and rotating discs

X-ray diffraction (XRD) patterns were collected on Bruker AXS D8 Advance powder diffractometer with Cu Kα radiation. The 2θ values (ranging from 20° to 100°) in steps of 0.1° and times in steps of 1 s were selected to analyse the crystals' structure and to estimate the crystallite size by means of the Scherrer equation [31] from the full-width at half-maximum of the XRD peaks [32].

For crystals' morphology, size, and aggregation examination, the SEM photographs of the probes were taken using scanning electron microscope (Hitachi S 5500 SEM/STEM with cold field emission gun).

Particles' (aggregates) size was examined using a 90 Plus Nanoparticle Size Analyzer (the wavelength of the laser: 657 nm) obtained from Brookhaven Instruments Co., which employs the dynamic light-scattering (DLS) method for the determination of effective diameter of the particles and multimodal size distribution. Every measurement was made at 25 °C with scattering angle being equal to 90°. The effective diameter of the particles was examined just after the precipitation process. The suspensions, prepared by dispersing 5 mg of $CaCO_3$ powder into buffer solutions (pH 7.0) at 25 °C, were filtered to remove all the impurities using wheel filter with pore size of 1 μm.

The purity analyses were carried out by means of TG Du Point Instruments. Argon used in the experiments was taken directly from a gas bottle (99.999 % pure, from Linegal, Poland). The constant inflow of the gas was maintained by means of mass flow controller MFC and was equal to 6 l h^{-1}. The samples were heated from 25 to 620 °C with the speed equal to 10 degrees per minute.

Results

Crystalline structure

The XRD analysis shows that, independent of the speed of rotation and the initial concentration of $Ca(OH)_2$, the polymorphic modification of the obtained $CaCO_3$ powder is of very high purity and of single calcite. In Fig. 2, independent of the initial concentration of $Ca(OH)_2$ and the disc's speed of rotation, the experimental results agree very well with the standard calcite data (the green bars on the diagram).

Thus, in the investigated system, only the most thermodynamically stable structure is formed. Although, in many cases, the precipitate is a mixture of two or three $CaCO_3$ polymorphs [33, 34], the obtained polymorphic form of $CaCO_3$ fully agrees with our previous results [24, 25].

The approximation of single crystal diameter has been calculated from the XRD patterns [32] using Scherrer equation (Eq. 1) [31]. The diameter, depending on the disc's speed of rotation and the initial $Ca(OH)_2$ concentration, varied from 32.1 to 35.2 nm.

$$d = 0.9\frac{\lambda}{\Delta\theta\cos\theta} \quad (1)$$

where d is the crystallite size (diameter), λ is the length of X-ray radiation, θ value of the diffraction reflex angle, and $\Delta\theta$ is the width of the diffraction peak in the middle of its height.

Because of the very small (almost equal to the calculation error) diameter differences, it is impossible to find a relation between process conditions (the disc's speed of rotation and the initial $Ca(OH)_2$ concentration) and the size of the obtained single crystals. Generally, we can say that under low mixing rate, the high supersaturation degree occurs in the liquid film on disc's surface and smaller crystallites can be formed, and when discs rotate with higher speed the liquid film is renewed faster and so the supersaturation degree is not achieved, which results in slightly larger crystallites; the size difference, in this case can, however, be neglected. The formation of single

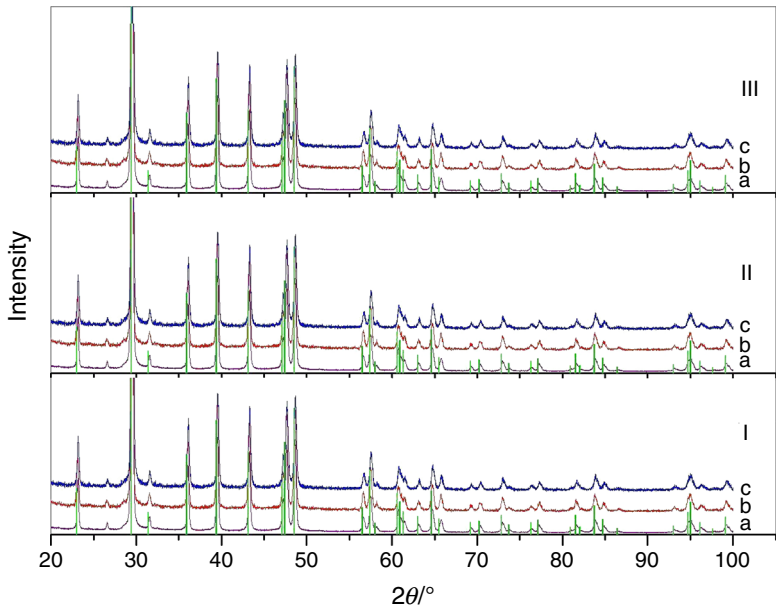

Fig. 2 The XRD patterns of $CaCO_3$ samples precipitated in RDR for initial $Ca(OH)_2$ concentrations equal to (*I*) 23 mM L^{-1}, (*II*) 54 mM L^{-1}, (*III*) 110 mM L^{-1} and disc's speeds of rotation equal to *a* 80 rpm, *b* 120 rpm, and *c* 160 rpm, together with standard calcite data

crystals with constant diameter, independent of the process conditions, can be explained by the large differences in the nucleation and aggregation rates. As was shown previously [25], the size of the obtained nanocrystals is strictly determined by the effective nucleic size. During the process times (14–18 min for 30 rpm; 7–9 min for 120 rpm), the crystals can grow only negligibly compared with the nucleic size.

Figure 3 shows the SEM micrographs of powders, taken several minutes after the end of precipitation reaction, obtained for different mixing conditions (different speeds of rotation of discs) and initial $Ca(OH)_2$ concentrations.

$CaCO_3$ crystals form aggregates of crystallites, which slightly differ in size and shape. The average size of the aggregate is in the range of 200–400 nm. It is seen also that the single crystallite size is evidently much lower that the size of the aggregates. Moreover, looking at the aggregates it is difficult to find a relation between process condition (different speeds of rotation of discs, initial $Ca(OH)_2$ concentrations) and their shape. However, particles from the lowest disc's speed of revolutions (Fig. 3a, b) are characterized by almost perfect rhombohedral morphology. When the mixing rate increases (Fig. 3c–f), the edges and corners start to be rounded up, but all the particles are of similar size.

Thermal analysis of calcite

The thermogravimetric (TG) curves of calcite obtained in the reactor with rotating disc are presented in Figs. 4–6. Generally, in TG experiments of calcite there are two regions of mass loss. The first is associated with a loss of contaminants and the second with the thermal decomposition of calcite which begins (in the case of pure calcite) at about 570 °C [35]. In our experiments the first region of mass loss (between 92 and 500 °C) can be further divided into two sub-regions: from 92 to 400 °C and from 400 to 500 °C. The first sub-region shows three mass losses connected (started from the lowest temperature) with desorption of adsorbed water, impurities of the initial reactants used (mainly impurities of $Ca(OH)_2$) and beginning of the decomposition of untransformed calcium hydroxide while the second sub-region corresponds probably to mass loss of the rest untransformed $Ca(OH)_2$. This interpretation should be treated only qualitatively because different effects overlap and the exact determination of the temperature range corresponding to the mass loss of each effect is impossible.

The peak of impurities coming from the initial reactants is visible in all Figures (Figs. 3–6) while the second peak, referring to the $Ca(OH)_2$, can be seen only for the $Ca(OH)_2$ initial concentration equal to 23 mM L^{-1} and 54 mM L^{-1} (Figs. 3, 4). Furthermore, the examined calcite decomposition temperature increases with decreasing of the level of impurities. The amount of the impurities which were adsorbed on the surface of calcite obtained in the rotating disc reactor at 80 rpm and different slurry concentrations together with the beginning of the calcite decomposition temperature are given in Table 1.

Figure 7 shows TG trace for $CaCO_3$ obtained at 80 rpm and the initial concentration of $Ca(OH)_2$ equal to 110 mM L^{-1} after its 2 h heating up in the laboratory oven

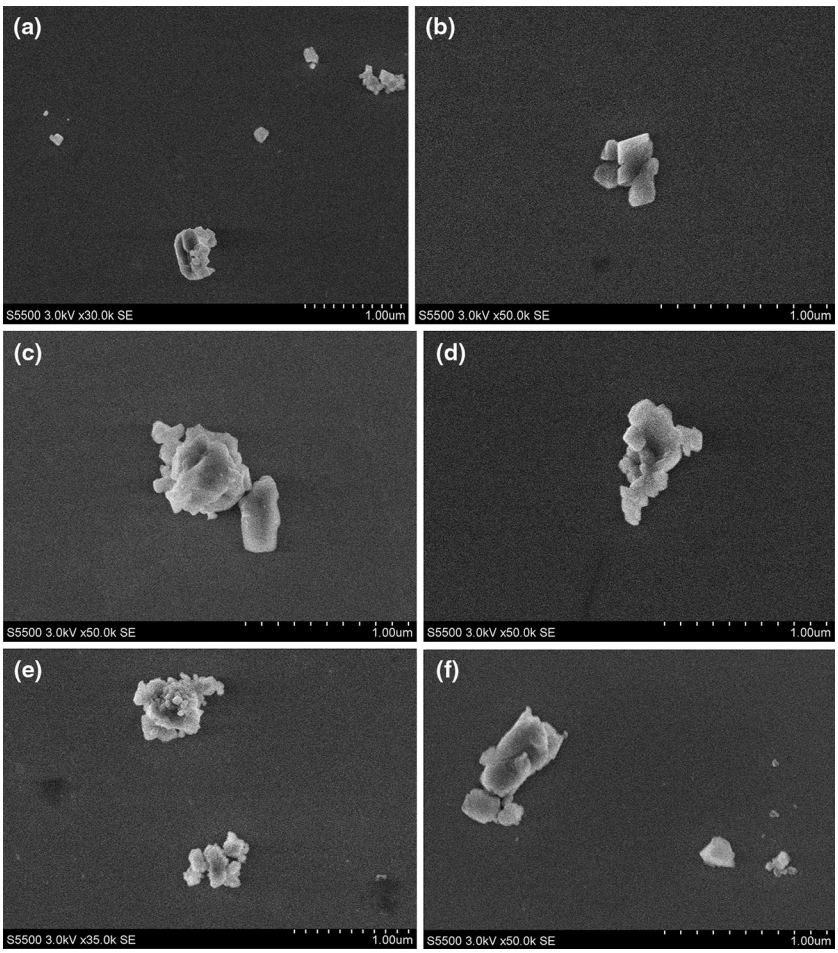

Fig. 3 The SEM micrographs of powders obtained in the reactor with rotating discs: **a** disc's speed of rotation—80 rpm, initial $Ca(OH)_2$ concentration—23 mM L^{-1}; **b** disc's speed of rotation—80 rpm, initial $Ca(OH)_2$ concentration—54 mM L^{-1}; **c** disc's speed of rotation—120 rpm, initial $Ca(OH)_2$ concentration—23 mM L^{-1}; **d** disc's speed of rotation—120 rpm, initial $Ca(OH)_2$ concentration—54 m mM L^{-1}; **e** disc's speed of rotation—160 rpm, initial $Ca(OH)_2$ concentration—23 mM L^{-1}; **f** disc's speed of rotation—160 rpm, initial $Ca(OH)_2$ concentration—54 mM L^{-1}

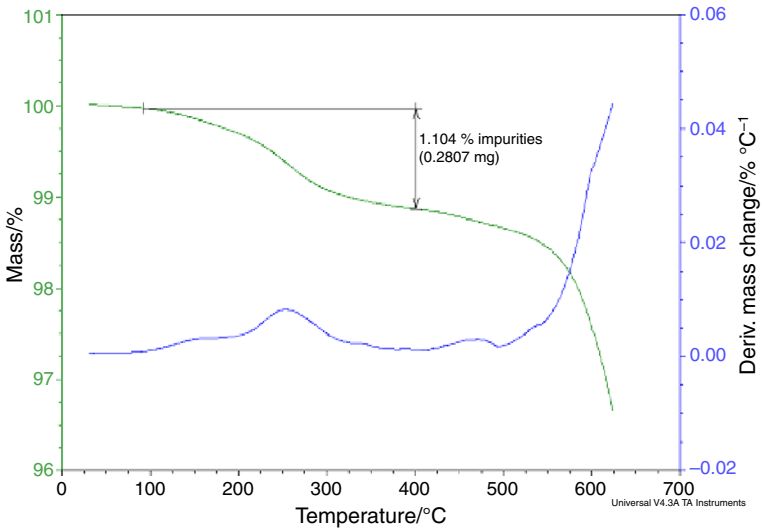

Fig. 4 TG trace for $CaCO_3$ obtained at 80 revolution speed rate by means of initial $Ca(OH)_2$ concentration equal to 23 mM L^{-1}

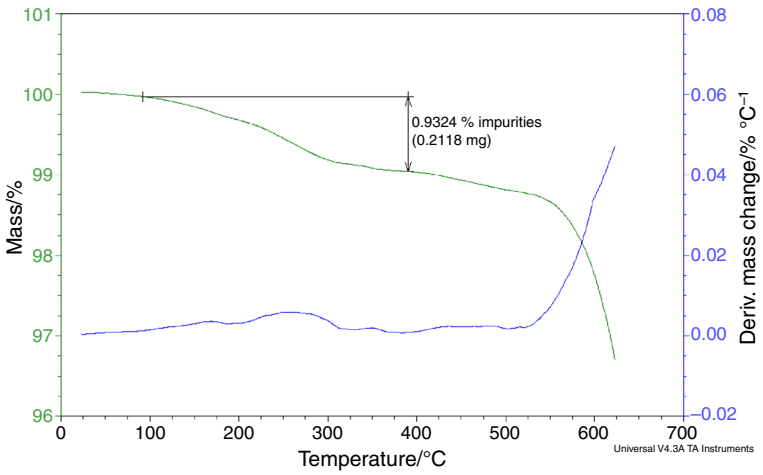

Fig. 5 TG trace for $CaCO_3$ obtained at 80 revolution speed rate by means of initial $Ca(OH)_2$ concentration equal to 54 mM L^{-1}

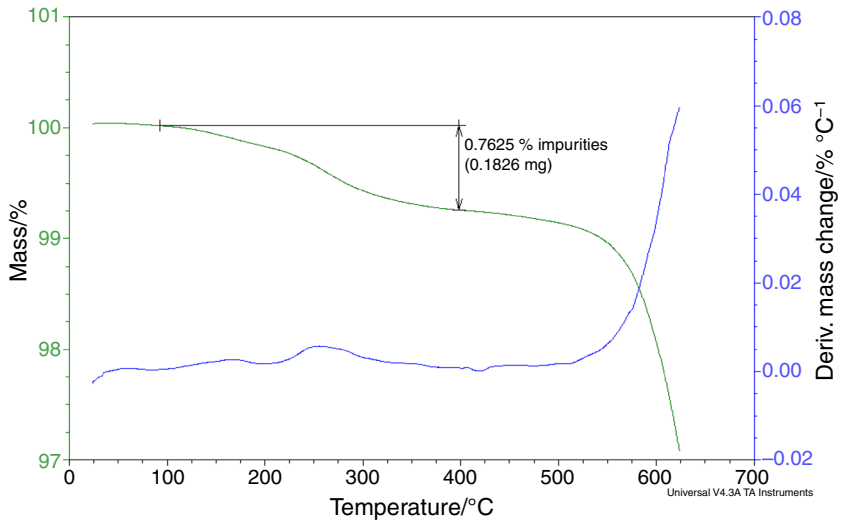

Fig. 6 TG trace for $CaCO_3$ obtained at 80 revolution speed rate by means of initial $Ca(OH)_2$ concentration equal to 110 mM L^{-1}

Table 1 Amount of the impurities which were adsorbed on the surface of calcite obtained in rotating disc reactor at 80 rpm and different slurry concentrations

Gas–liquid contact area/m^2 g^{-1}	Initial $Ca(OH)_2$ concentration/mM L^{-1}	Reaction time/min	Loss of mass/%	Temperature/°C		Start of decomposition calcite/°C
				Initial	Final	
0.12	23	8	1.104	92.38	401.17	495.5
	54	11	0.9324	91.49	390.49	501.7
	110	15	0.7625	92.38	398.50	507.1

to 400 °C. As a result all the impurities were removed and the sintering of calcite particles was not seen. Moreover, the initial temperature of calcite decomposition was shifted of about 50 °C (from 507.1 to 556.0 °C). So the decomposition starts close to the temperature of decomposition of "normal" (non-nano) size of calcite [35–37].

The effect of calcite particle size on the decomposition parameters was studied before [1, 38, 39]. The research carried out by Yue et al. [1] showed a downward shift in the decomposition temperature (~50 °C) for nanophase compared to the normal size of calcite. In another TG analysis [38], the shift of temperature was not seen and no

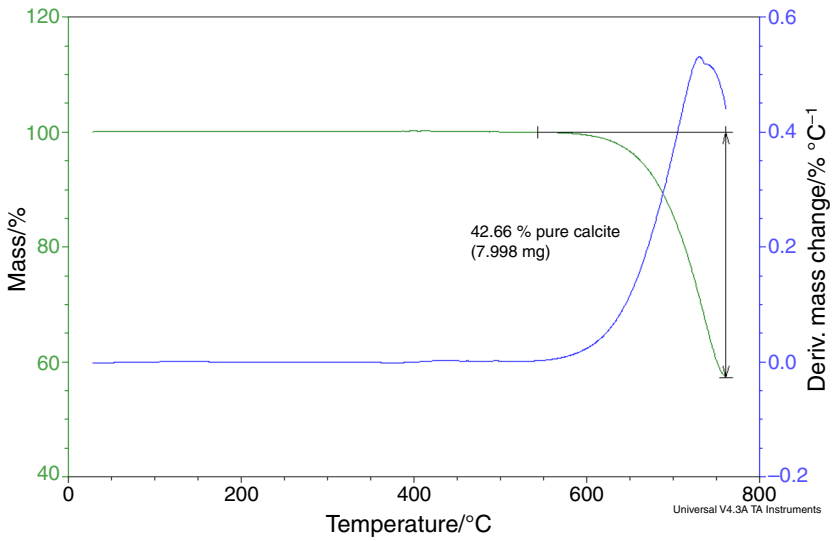

Fig. 7 TG trace for $CaCO_3$ obtained at 80 revolution speed rate by means of initial $Ca(OH)_2$ concentration equal to 110 mM L^{-1} and heated up to 400 °C in laboratory oven

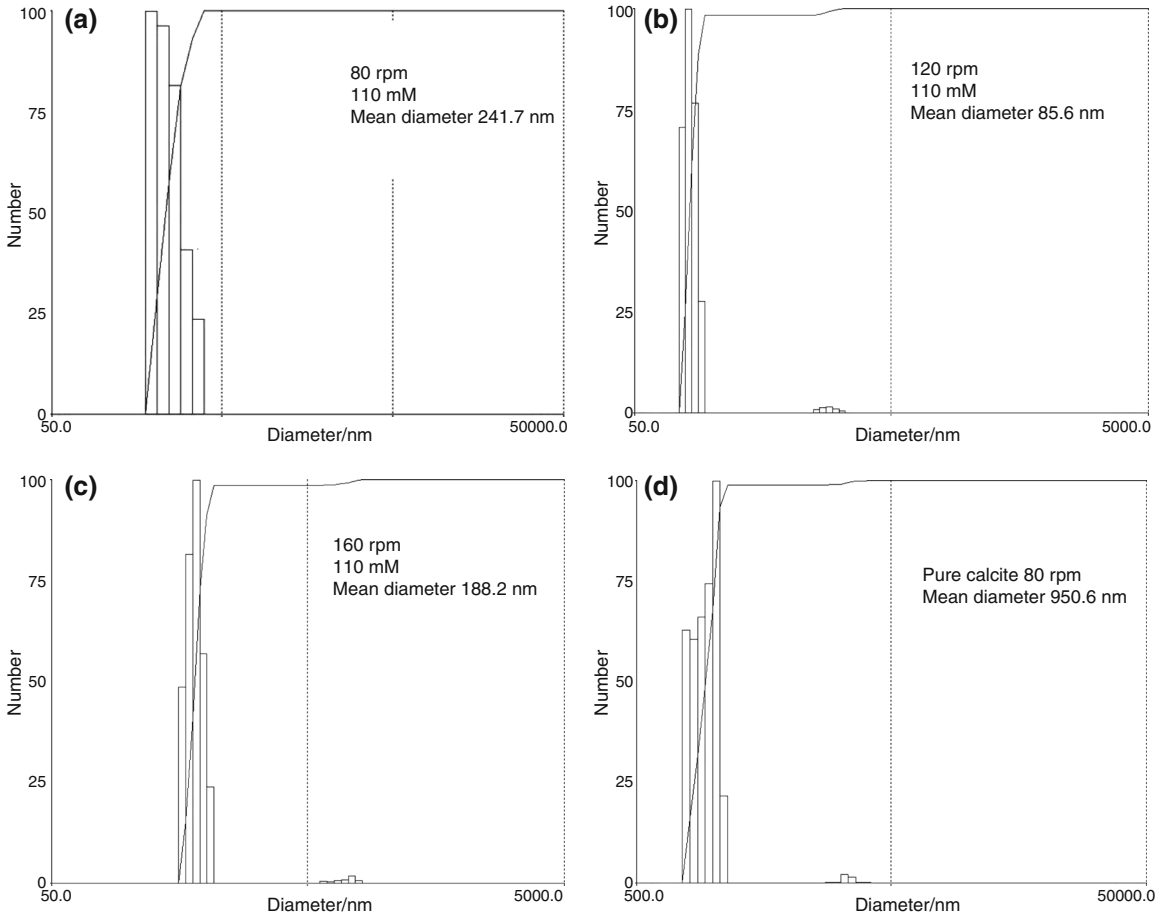

Fig. 8 Aggregate size distribution obtained by means of the DLS method for $CaCO_3$ precipitated in the reactor with rotating discs, for initial $Ca(OH)_2$ concentration 110 mM L^{-1} and revolution speeds of discs equal to **a** 80 rpm, **b** 120 rpm, **c** 160 rpm and **d** 80 rpm (further purified calcite)

significant trend in the TG experiments was found. Generally, it can be stated [1, 38, 39] that the beginning of calcite decomposition depends on the form of calcite (single crystals, powder, etc.) and in the case of nanocrystals can be moved downward for about 50–80 °C.

Aggregate size and aggregation time

The distributions of aggregate size in the output suspensions obtained immediately after the end of reaction, from the reactor with rotating discs, for initial concentration of $Ca(OH)_2$ equal to 110 mM L^{-1} are presented in Fig. 8.

By looking at the obtained results, it is seen that for initial $Ca(OH)_2$ concentration equal to 110 mM L^{-1}, the distribution of aggregates is mostly monomodal (Fig. 8a, b, c, d). At low mixing rate (80 rpm), the average size of the aggregates was 241.7 nm (Fig. 8a), and it decreased for higher mixing condition (120 rpm) to 85.6 nm (Fig. 8b). Further increase in the mixing rate to 160 rpm, which decreased the reaction time, did not cause the decrease in the aggregate diameter (diameter equal to 188.2 nm). It is very difficult to give the unequivocal explanation of the obtained aggregate size's dependence on the process conditions (the disc's speed of rotation and the initial $Ca(OH)_2$ concentration). The obtained results can be roughly explained by the fact that, at low mixing rate, the high supersaturation degree occurs in the liquid film on disc's surface and smaller crystallites can be formed and when the discs rotate with higher speed, the liquid film is renewed faster, so the supersaturation degree is not achieved which results in slightly larger crystallites (Fig. 8c). The different sizes of crystallites, different disc's speeds of rotation and different times of reaction influence the aggregates' formation, which results in their different average sizes for different mixing conditions (for the same $Ca(OH)_2$ initial concentration). It is necessary to notice that the time of reaction is linked with the disc's speed of rotation, but there is no quantitative correlation between these two parameters. Moreover, at higher mixing rates, the equilibrium condition in the film is not reached. So, taking into account all these factors, it is impossible to provide, as it was stated above, the unequivocal explanation of the relation between the size of aggregates formed in the RDR and the process parameters.

The size of the aggregates was also measured after heating them up in the laboratory oven. After few hours of heating (for the removal of the impurities), the average diameter of agglomerates became equal to 950.6 nm. The aggregates' size distribution was almost monomodal, similar to those obtained immediately after the end of reaction (Fig. 8).

Table 2 Influence of reaction time, disc's speed of rotation and initial concentration of the slurry on the diameter of the particles

Initial $Ca(OH)_2$ concentration/mM L^{-1}	Disc's speed of rotation/rpm	Reaction time/min	Diameter/nm
110	80	15	241.7
	120	11	85.6
	160	9	188.2
54	80	11	219.4
	120	9	70.3
	160	7	146.2

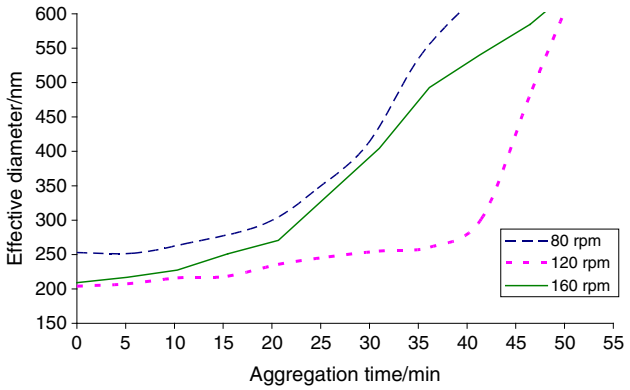

Fig. 9 Aggregation of the $CaCO_3$ particles in time, after the end of reaction, for initial $Ca(OH)_2$ concentration equal to 110 mM L^{-1} and different mixing conditions (80, 120 and 160 rpm)

The results showing influence of the reaction time, disc's speed of rotation and initial concentrations of the slurry on the aggregates diameter are shown in Table 2.

Figure 9 shows the change of calcite aggregates' size over time, after the end of reaction, for three different mixing conditions. The effective diameter of the aggregates, leaving in the solution after the end of reaction, strongly depends on time. The agglomerates grow during the time of being in the solution.

The initial effective diameter, independent of the mixing conditions, is equal to ca. 250 nm (252.8 nm for 80 rpm, 204 nm for 120 rpm and 201.3 nm for 160 rpm—Fig. 9) but it is stable only for a short time. The time for which the average size of agglomerates is in the range of 200–250 nm depends on the mixing rate (Fig. 9). For the lower (80 rpm) disc's speed of rotation this time is equal to 20 min and for higher (160 rpm) speed of disc's rotation the time is equal to about 45 min. The shorter formation time of stable agglomerates for 80 rpm compared to 120 rpm can be explained by the fact that, as was mentioned before, at low mixing rate (80 rpm), due to high supersaturation degree in the liquid film, the smaller crystallites are formed, which leads to faster agglomeration than the slightly larger particles obtained for 120 rpm. The formation time of stable

agglomerates for 160 rpm is only slightly longer than that in the case of 80 rpm and much shorter than that for 120 rpm. It is caused by the fact that when discs rotate at such a high rate, the liquid film is quickly renewed, and the supersaturation degree is not achieved (non-equilibrium) as well as due to the non-homogenous mixing which affects the reaction kinetics, leading to the formation of agglomerates of such a size (similar to that for 80 rpm). Moreover, from Fig. 9, it is seen that, in this case (160 rpm), the agglomerates grow at a faster rate (slope of the line—Fig. 9) than those in the cases of both the other (80 rpm and 120 rpm) mixing rates.

After the stable period, the aggregates start to grow very quickly (Fig. 9). The agglomerates of particles obtained for 80 rpm reach the size of 600 nm after 35 min, while those obtained both for 120 rpm and 160 rpm reach the same after 50 min. Times of the increase from the stable period to reach the size of 600 nm are almost the same for 80 rpm and 120 rpm, while in the case of 160 rpm, the time is almost twice longer. Moreover, the character of agglomeration (slope of the agglomeration curve—Fig. 9) in the case of 160 rpm is completely different from that for the two other mixing rates, which confirms our assumption concerning different kinetics of the aggregates formation.

Further, agglomeration of particles, which takes place when the aggregate's size exceeds 600 nm, causes falling down of the aggregates, which results in a large fluctuation in the measured values of the effective diameters. After a few hours, the average diameter of the agglomerates, as was mentioned above, is approximately equal to 950 nm. It is necessary to point out also that according to bimodal distribution of the particles (Fig. 8), some of the aggregates (with high initial size), during the 25–50 min, reach the size exceeding 1,000 nm and then fall down thus influencing the measurements of the aggregate's size.

The model and simulation results

The previously elaborated model [25] very accurately described the size of single $CaCO_3$ nanocrystals obtained in the rotating disc reactor. We assumed that the reaction proceeds in the thin liquid film formed on the surface of the rotating disc [25], which creates a constant surface area of gas–liquid interface, and the carbonation reaction of lime water involves gas, liquid and solid phase. So, the process can be described by the four following reactions:

$$CO_{2(g)} = CO_{2(l)} \quad (2)$$

$$CO_{2(g)} + OH^- = HCO_3^- \quad (3)$$

$$HCO_3^- + OH^- = CO_3^{2-} + H_2O \quad (4)$$

$$Ca^{2+} + CO_3^{2-} = CaCO_{3(s)} \quad (5)$$

For the calculation of the mass balance of these reactions, we applied the film theory [40, 41]:

$$\frac{\partial c_{CO_2}}{\partial t} = D_{CO_2}\left(\frac{\partial^2 c_{CO_2}}{\partial x^2}\right) - k c_{CO_2} c_{OH} \quad (6)$$

$$\frac{\partial c_{OH}}{\partial t} = D_{OH}\left(\frac{\partial^2 c_{OH}}{\partial x^2}\right) - k c_{CO_2} c_{OH} \quad (7)$$

$$\frac{\partial c_{CaCO_3}}{\partial t} = D_{CaCO_3}\left(\frac{\partial^2 c_{CaCO_3}}{\partial x^2}\right) - k c_{CO_2} c_{OH} - G' - B' \quad (8)$$

where t is the time; c_{CO_2}, c_{OH} and c_{CaCO_3} are the concentrations of gas reactant [$CO_{2(g)}$], liquid reactant [OH^-] and the product [CO_3^{2-}], respectively; G' and B' are the rates of nucleation and crystal growth, respectively; k is the second-order chemical reaction constant; D_{CO2}, D_{OH} and D_{CaCO3} are the diffusivity values of ($CO_{2(g)}$), (OH^-) and (CO_3^{2-}), respectively;

The population balance of the precipitated particles ($CaCO_3$) was described, assuming that the concentration of [CO_3^{2-}] is constant across the diffusion layer, by the following equation [42]:

$$\frac{\partial N}{\partial t} + G\left(\frac{\partial N}{\partial L}\right) = D_P\left(\frac{\partial^2 N}{\partial x^2}\right) \quad (9)$$

where N is the population density of particles, G is the linear growth rate, L is the coordinate of particle dimension, and D_P is the diffusivity of particles.

After substituting

$$N = P/L, \quad (10)$$

we get that

$$\frac{\partial P}{\partial t} + G\left(\frac{\partial P}{\partial L}\right) = D_P\left(\frac{\partial^2 P}{\partial x^2}\right) + \frac{G}{L}P \quad (11)$$

where $P(x,L_i)$ is the number of density discretized, L_i is the particle size coordinate, and L_0 is the effective nucleic size, for the newly nucleated particles.

Solving the mass balance equations (Eqs. 6–8) and the population equation (Eq. 11) (with the proper boundary conditions [25]), we could calculate the discretized density number of particles ($P(t,x,L_i)$) and the discretized diameter L_i.

To calculate the size of the aggregates obtained in the rotating disc reactor, we decided to extend our model adding to the population balance the term describing aggregation and disaggregation processes. So, when $D_p = \text{const}$, Eq. (9) can be rewritten in the following form [43]:

$$\frac{\partial N}{\partial t} + G\left(\frac{\partial N}{\partial L}\right) = D_P\left(\frac{\partial^2 N}{\partial x^2}\right) + S \quad (12)$$

where S is the function describing aggregation and disaggregation rates.

The S function (dependent on volume) can be generally written as two different functions: function which describes aggregates' formation—$b(v)$ ("birth") and function which describes their disappearance—$d(v)$ ("death").

$$S(v) = b(v) - d(v) \tag{13}$$

Both functions ($b(v)$ and $d(v)$) consist of two contributions concerning aggregation of particles ($b_a(v)$ *i* $d_a(v)$) as well as their disaggregation ($b_d(v)$ *i* $d_d(v)$). In the case of particles' aggregation, we deal, at the same time, both with the formation and disappearance of aggregates because from many small aggregates (which disappear—$d_a(v)$), larger aggregates (formation of new particles—$b_a(v)$) are formed. The same situation is obtained in the case of aggregates' disappearance—the large aggregates disappear ($d_d(v)$), and new small aggregates are formed (formation of new particles—$b_d(v)$) Thus,

$$S(v) = b_a(v) + b_d(v) - d_a(v) - d_d(v) \tag{14}$$

We can assume further, that in the case of calcium carbonate precipitation (weakly dissolved salt), aggregation determines size of the particles, and thus the disappearance process can be omitted in our considerations [44]. This assumption is especially correct for the crystallization process taking place in the rotating disc reactor because of the high supersaturation of the solution and the short time of the process. After this assumption, Eq. (14) will have the following form:

$$S(v) = b_a(v) - d_a(v) \tag{15}$$

where, for the initial aggregation condition [44],

$$n(v, t = 0) = n_o(v); \tag{16}$$

the $b_a(v)$ and $d_a(v)$ contributions assume the following forms:

$$b_a(v) = \int_0^V \beta(v - v', v')n(v - v')n(v')\mathrm{d}v' \tag{17}$$

$$d_a(v) = n(v)\int_0^\infty \beta(v, v')n(v')\mathrm{d}v' \tag{18}$$

where $\beta(v,v')$ is the aggregation rate (frequency of collision of particles of volume v with particles of volume v'), and $n(v)$ is the number of particles of volume v.

Equations (17, 18) can be expressed, instead of a volume function, in the form of a function of the particle size coordinates:

$$b_a(L) = \frac{L}{2}\int_0^L \beta((L^3 - \lambda^3)^{1/3}, \lambda)n(L - \lambda)n(\lambda)\mathrm{d}\lambda \tag{19}$$

$$d_a(L) = n(L)\int_0^\infty \beta(L, \lambda)n(\lambda)\mathrm{d}\lambda \tag{20}$$

where $\beta(L,\lambda)$ is the aggregation rate (frequency of collision of particles of size L with particles of size λ), and $n(L)$ is the number of particles of size L.

Substituting Eqs. (19, 20) into Eq. (15), we get the final form of function (S) describing particles' aggregation in the rotating disc reactor:

$$S(L) = \frac{L}{2}\int_0^L \beta((L^3 - \lambda^3)^{1/3}, \lambda)n(L - \lambda)n(\lambda)\mathrm{d}\lambda - n(L)\int_0^\infty \beta(L, \lambda)n(\lambda)\mathrm{d}\lambda \tag{21}$$

Crystal growth and aggregation are strongly dependent on the supersaturation of solution. If we assume that, according to Rigopoulos and Jones [3], because of the supersaturation of the solution in the rotating disc reactor, the expressions describing crystal growth and their aggregation should have the same rates, then the aggregation rate can be expressed by the following equation:

$$\beta((L - \lambda), \lambda) = k_a(\lambda_s - 1)^g(\lambda + (L^3 - \lambda^3)^{1/3}) \tag{22}$$

where k_a is the aggregation constant [3], λ_s is the solution supersaturation rate, and g is the order of crystal growth.

Solution's supersaturation rate (ions in solution) can be expressed by the following equation [45]:

$$\sqrt{\lambda_s} - 1 = \sqrt{\frac{a_{Ca+}a_{CO_3-}}{K_{sp}}} - 1 \tag{23}$$

where a_{Ca+} and a_{CO_3-} are the ion activities of the Ca^{2+} and $CO_3{}^{2-}$, respectively; and K_{sp} is the solubility of the product (calcium carbonate).

Ions' activities can be calculated from the modified [46] Debye–Hückel equation:

$$a_i = \gamma_i c_i \tag{24}$$

$$\log\gamma_i = -A_{DH}z_i^2\left(\frac{\sqrt{I}}{1 + \sqrt{I}} - 0.3I\right) \tag{25}$$

where γ_i is the activity of ion i, c_i is the concentration of ion i, I is the ionic strength, z_i is the charge of ion i and A_{DH} is the Debye–Hückel constant

The ionic strength is described by the following equation:

$$I = \frac{1}{2}\sum_i z_i^2 c_i \tag{26}$$

Solving the mass balance equations (Eqs. 6–8) and population equation (Eqs. (11, 12) we could calculate the discretized density number of particles ($P(t,x,L_i)$) and discretized diameter L_i.

To perform simulation calculations, we need some expressions concerning diffusivity of particles, rates of nucleation and crystal growth, and boundary conditions. In the extended model, we assume, for the above variables, the same expressions as in the previous one [25].

The diffusivity of the crystals within the liquid film was described by the Stokes–Einstein equation [47]:

$$D_{\mathrm{P}} = k_{\mathrm{B}}T/(6\pi\mu r) \tag{27}$$

where k_{B} is the Boltzmann constant, $k_{\mathrm{B}} = 1.38\ 10^{-23}$ [kg m^2 s^{-2} K^{-1}], T is the temperature [K], μ is the viscosity [P] and r is the radius of particle.

The number rate of nucleation (J_{n}) and linear crystal growth (G) were expressed by the Nielsen equations [48]:

$$J_{\mathrm{n}} = k_{\mathrm{n}}(C - C^*)^n \tag{28}$$

$$G = k_{\mathrm{g}}(C - C^*)^g \tag{29}$$

where n and g are the orders of nucleation and growth, respectively; C and C^* are the concentration and equilibrium saturation concentration, respectively; and k_{n} and, k_{g} are the nucleation and growth rate constants, respectively.

The above equations can be expressed in the following forms:

$$J_{\mathrm{n}} = k_{\mathrm{n}}\left(\sqrt{c_{\mathrm{Ca}}c_{\mathrm{CO_3}}} - \sqrt{K_{\mathrm{sp}}}\right)^{\mathrm{n}} \tag{30}$$

$$G = k_{\mathrm{g}}\left(\sqrt{c_{\mathrm{Ca}}c_{\mathrm{CO_3}}} - \sqrt{K_{\mathrm{sp}}}\right)^{\mathrm{g}} \tag{31}$$

The corresponding mass based rate equations of nucleation and growth are respectively:

$$B' = \alpha\rho J_{\mathrm{n}}L_0^3 \qquad (\alpha = \pi/6 \text{ for the sphere}) \tag{32}$$

$$G' = \sum_{i=0}^{\infty} \beta\rho P(x, L_{\mathrm{i}})GL_{\mathrm{i}}^2 \qquad (\beta = \pi \text{ for the sphere}) \tag{33}$$

where ρ is the crystal density

The boundary conditions for the gas–liquid interface, assuming that, except for the gaseous reactant ($CO_{2(g)}$), every component is non-volatile, are as follows:

$$\begin{aligned} x = 0; t > 0 \rightarrow c_{\mathrm{CO_2}} = c^0_{\mathrm{CO_2}}, \mathrm{d}c_{\mathrm{OH}}/\mathrm{d}x = 0, \\ \mathrm{d}c_{\mathrm{CO_3}}/\mathrm{d}x = 0, \mathrm{d}P/\mathrm{d}x = 0, \end{aligned} \tag{34}$$

and for the film formed on the disc's surface (δ_{F}—film thickness), assuming that the newly nucleated particles have an effective nucleic size equal to L_0, they are as follows:

Table 3 Parameters' values used for the simulation

Parameter	Value	Reference
k_n	1.0×10^7 mol^{3n-3} s^{-1}	[49]
n	4.2	
k_g	8.06×10^{-9} mol^{-g} m^{3g+1} s^{-1}	[50]
g	2.0	
$D_{\mathrm{CO_2}} = D_{\mathrm{OH}} = D_{\mathrm{CaCO_3}}$	2.2×10^{-9} m^2 s^{-1}	[51]
K_{sp}	3.47×10^{-3} mol^2 m^{-6}	[52]
k	12.4 m^3 s^{-1} mol^{-1}	[53]
ρ	2.71 g cm^{-3}	[54]

$$\begin{aligned} &\text{at } t > 0, \quad 0 < x < \delta_F; \quad t > 0; \rightarrow L = L_0\frac{\partial P}{\partial t} + G\left(\frac{\partial P}{\partial L}\right) \\ &= D_{\mathrm{P}}\left(\frac{\partial^2 P}{\partial x^2}\right) + J_n + S \end{aligned} \tag{35}$$

$$L \rightarrow \infty; P = 0 \tag{36}$$

Simulations of the aggregation of $CaCO_3$ nanoparticles obtained in the rotating disc reactor, according to the above model, have been performed under the following assumptions:

(1) The concentration of $Ca(OH)_2$ in the aqueous solution is defined by its solubility in water and kept at constant level until the excess of solid $Ca(OH)_2$ is not exhausted. Then, the dissolved $Ca(OH)_2$ level decays exponentially;
(2) The gaseous CO_2 concentration is kept at constant level, and its concentration in water is defined by its solubility in water;
(3) The dissolved form of $CaCO_3$ precipitates according to kinetic laws described in the model, when its concentration exceeds the saturation level;
(4) The increase of the obtained crystal mass is proportional to the entire area of the nucleus;
(5) The time intervals for the calculation of the nucleus formation, crystal growth and aggregation are equal to the time of disappearance of CO_2; and
(6) The change of the disc's speed of rotation is simulated by changingthe entire process time.

The nucleus formation is much faster than the growth of the crystals. To account for this, the following two loops have been created in the simulation program: the outer loop which updates the size of precipitated grains and the inner loop which updates the grain number of density.

All the physico-chemical parameters needed for the calculations are given in Table 3. The nuclei effective size

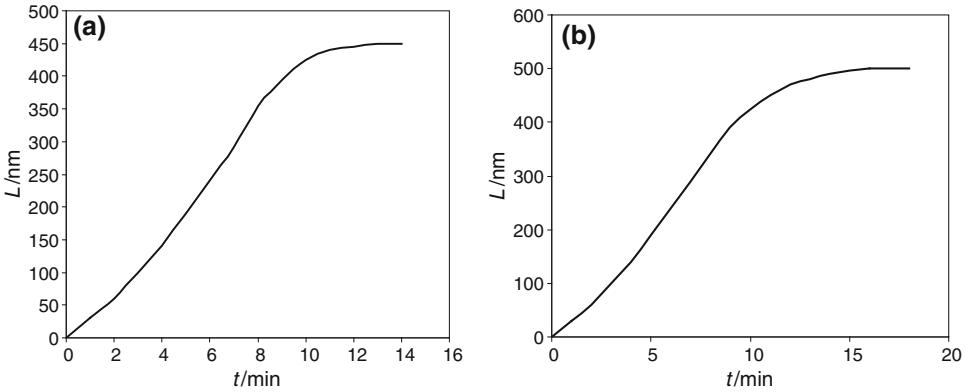

Fig. 10 Simulation results—the size of $CaCO_3$ aggregates as a function of the precipitation reaction time in the rotating disc reactor with disc's speed of rotation being equal to 30 rpm and initial $Ca(OH)_2$ concentration being equal to: **a** 23 mM L^{-1}, **b** 54 mM L^{-1}

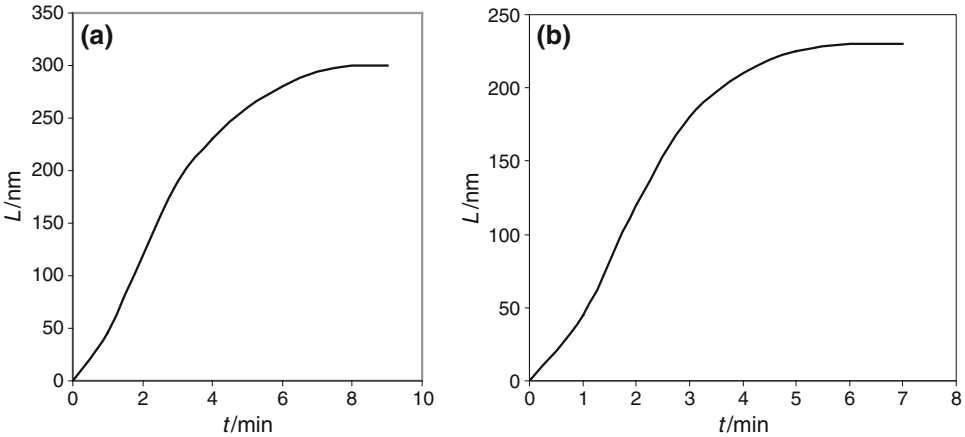

Fig. 11 Simulation results—the size of $CaCO_3$ aggregates as a function of the precipitation reaction time in the rotating disc reactor with disc's speed of rotation being equal to 80 rpm and the initial $Ca(OH)_2$ concentration being equal to **a** 23 mM L^{-1}, **b** 54 mM L^{-1}

L_0 was taken as equal to 30 nm (taken from the Gibbs–Thompson equation; according to S. Wachi and A.G. Jones' estimation [40], it varies from 10^{-8} to 5×10^{-8} m)—according to our previous simulations [25].

We have performed different simulations by changing the concentrations of $Ca(OH)_2$ (from 23 to 54 mM L^{-1}), and disc's speeds of rotation (from 30 rpm–14 min. for $Ca(OH)_2$ concentration = 23 mM L^{-1}; 18 min. for $Ca(OH)_2$ concentration = 54 mM L^{-1} to 80 rpm–7 min. for $Ca(OH)_2$ concentration = 23 mM L^{-1}; 9 min. for $Ca(OH)_2$ concentration = 54 mM L^{-1}).

Calculated sizes of the aggregates during the reaction for different $Ca(OH)_2$ concentrations (23 and 54 mM L^{-1}) are shown in Fig. 10 (disc's speed of rotation equal to 30 rpm) and 11 (disc's speed of rotation equal to 80 rpm).

Obtained simulation results (Figs. 10, 11) clearly show that, independent of disc's speed of rotation and initial $Ca(OH)_2$ concentration, aggregates' size growth in monotonic way during the process time. This leads to the formation of almost monomodal (similar average size) aggregates at the end of the process.

Aggregates' size depends most of all on the process time and is equal to ca.. 230 nm for the process lasting 7 min. (Fig. 11a), 300 nm for the process lasting 9 min. (Fig. 11b), 450 nm for the process lasting 14 min (Fig. 10a) and 500 nm for the process lasting 18 min. (Fig. 10b). The constant value of the aggregates obtained is due to the fact that, as was stated in our previous simulation (the limited model—[25]), single nanoparticle of $CaCO_3$ formed in the rotating disc reactor used has constant size (about 30 nm—[25]). That is why the aggregation constant (Eq. 20) and function describing aggregation process (Eq. 19) do not depend on the difference in particles size but are dependent on their number in the system (reactor).

Simulation results have been compared with the experimental values. Figures 12 and 13 show a comparison of the sizes of the aggregates precipitated in the rotating disc reactor obtained from the performed simulation with the experimental data obtained by means of DLS method.

The average sizes of aggregates, after the end of reaction measured by DLS method for the disc's speed of rotation equal to 30 rpm, were 425 nm (Fig. 12a) for the initial $Ca(OH)_2$ concentration—23 mM L^{-1} and 516 nm for the initial $Ca(OH)_2$ concentration—54 mM L^{-1} (Fig. 12b). In both cases, the particles size distribution was monomodal. However, the obtained aggregates can differ even by 80 nm. Increasing the disc's speed of rotation to 80 rpm caused decrease in the average size of the aggregates.

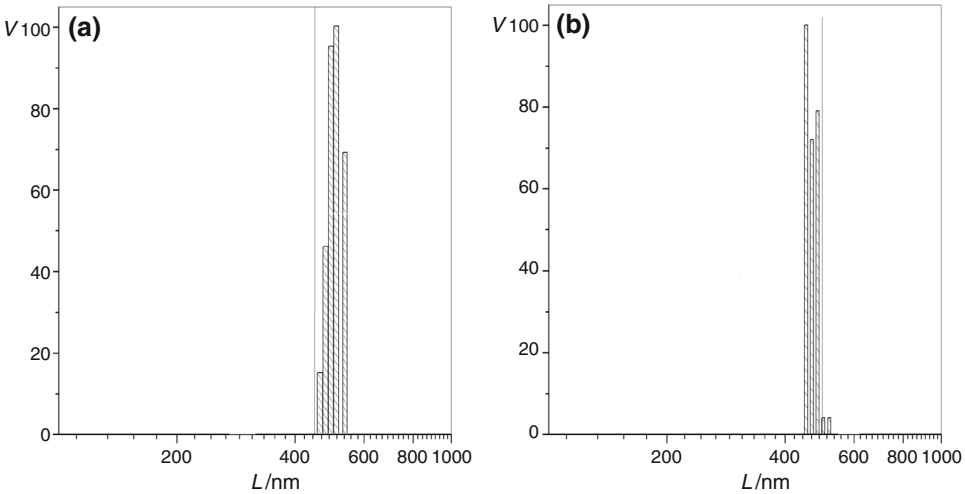

Fig. 12 Particle size distribution in the rotating disc reactor obtained from the performed simulation (*vertical straight line*) and by means of dynamic light scattering (DLS) method, with disc's speed of rotation being equal to 30 rpm and the initial $Ca(OH)_2$ concentration being equal to **a** 23 mM L^{-1}, **b** 54 mM L^{-1}

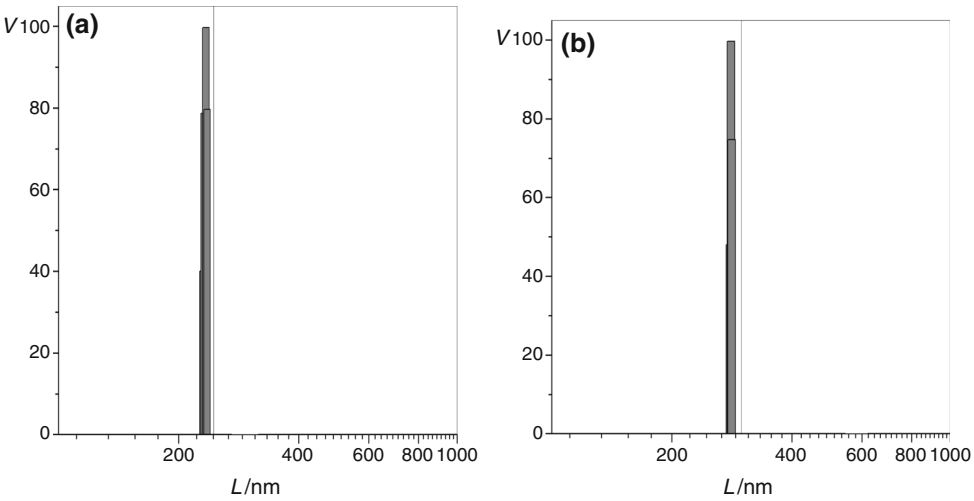

Fig. 13 Particle size distribution in the rotating disc reactor obtained from the performed simulation (*vertical straight line*) and by means of dynamic light scattering method with the disc's speed of rotation being equal to 80 rpm and the initial $Ca(OH)_2$ concentration being equal to: **a** 23 mM L^{-1}, **b** 54 mM L^{-1}

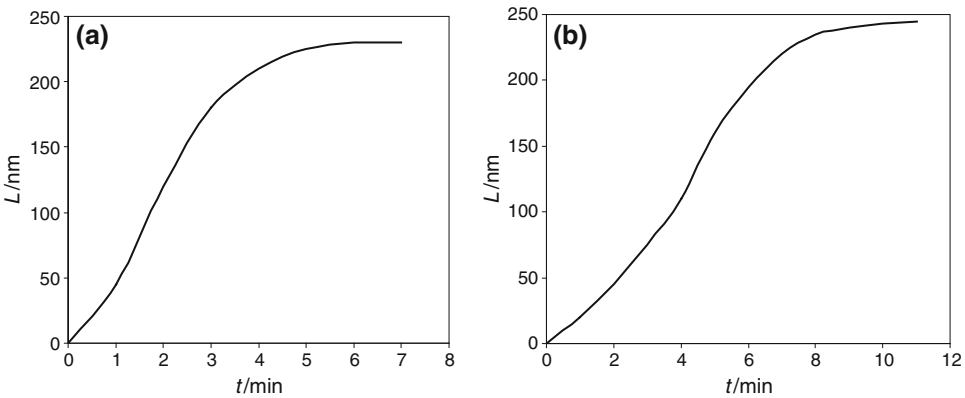

Fig. 14 Simulation results—the size of $CaCO_3$ aggregates as a function of the precipitation reaction time in the rotating disc reactor with disc's speed of rotation being equal to 80 rpm and the initial $Ca(OH)_2$ concentration being equal to: **a** 54 mM L^{-1}, **b** 110 mM L^{-1}

Again, the obtained aggregates were almost monodispersed, but their average size was reduced to 290 nm for the initial $Ca(OH)_2$ concentration equal to 23 mM L^{-1}, (Fig. 13a) and to 219 nm for the initial $Ca(OH)_2$ concentration equal to 54 mM L^{-1} (Fig. 13b).

We have performed also simulations for the investigated reaction conditions, i.e. the initial $Ca(OH)_2$ concentrations equal to 54 and 110 mM L^{-1} and three different speeds of rotation of the disc equal to 80, 120 and 160 rpm. The simulation results are shown in Figs. 14–16.

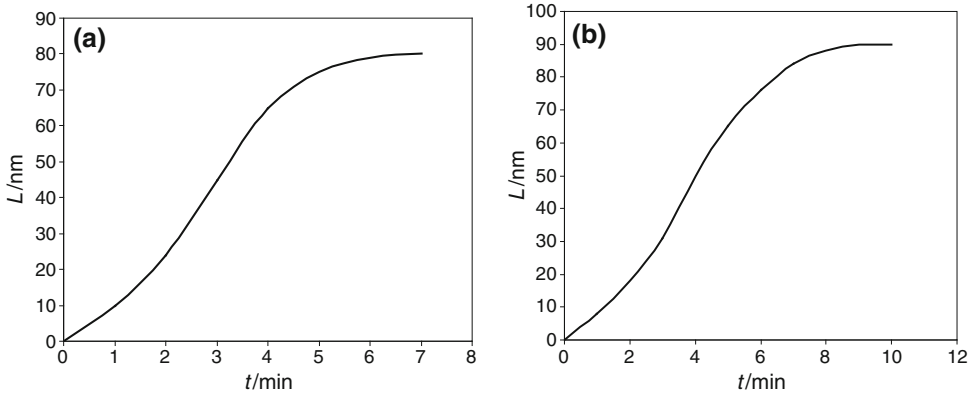

Fig. 15 Simulation results—the size of $CaCO_3$ aggregates as a function of the precipitation reaction time in the rotating disc reactor with disc's speed of rotation being equal to 120 rpm and the initial $Ca(OH)_2$ concentration being equal to **a** 54 mM L^{-1}, **b** 110 mM L^{-1}

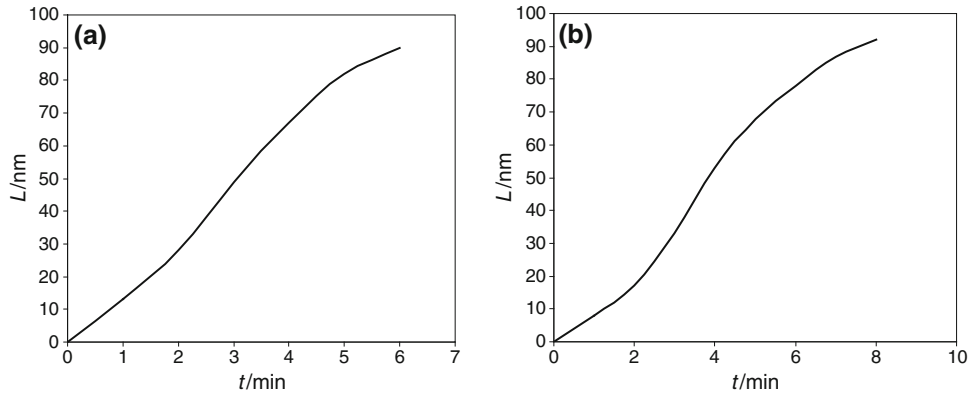

Fig. 16 Simulation results—the size of $CaCO_3$ aggregates as a function of the precipitation reaction time in the rotating disc reactor with disc's speed of rotation being equal to 160 rpm and the initial $Ca(OH)_2$ concentration being equal to **a** 54 mM L^{-1}, **b** 110 mM L^{-1}

Besides the results obtained for the disc's speed of rotation equal to 160 rpm (Fig. 16), the simulation results also fully agree with the experimental data (Table 2; Figs. 9—the initial effective size, 12, 13, 14, 15). The discrepancy between the final size of aggregates obtained from simulation (85 nm for initial $Ca(OH)_2$ concentration = 54 mM L^{-1} and 90 nm for initial $Ca(OH)_2$ concentration = 110 mM L^{-1}) and the experiment (146.2 nm for initial $Ca(OH)_2$ concentration = 54 mM L^{-1} and 188.2 nm for initial $Ca(OH)_2$ concentration = 110 mM L^{-1}) for the 160 rpm, can be caused by the fact that in the reactor, at such a high rate, the liquid film is quickly renewed, and the supersaturation degree is not achieved (non-equilibrium), which is not taken into account by the model. So, due to the non-homogenous mixing affecting the reaction kinetics experimentally, the formation of agglomerates with the size similar to that for 80 rpm takes place. It is worthy to notice that the shape of simulation curves for the disc's speed of rotation equal to 160 rpm (Fig. 16) shows that the equilibrium condition has not been reached.

In the case of the reactor used, independent of the process conditions, the monodispersed, nanometric single crystals (30 nm—[25]) have been obtained, which further agglomerate to form monomodal aggregates with the size depending on the disc's speed of rotation.

Summarizing the results of crystallization process performed in the rotating disc reactor, we can state that proposed (extended) model is internally consistent, and very well describes both the formation and the aggregation of calcite particles until the equilibrium condition is reached. Therefore, the model can be used and recommended for accurate calculations of the particles' and aggregates' sizes as well as their distribution obtained by gas–liquid precipitation reaction in the reactor. It is necessary to point out that the proposed model does not describe the nanoparticles' aggregation which takes place after the end of the precipitation reaction in the rotating disc reactor.

Conclusions

The results obtained in the study show that the carbonation of dispersed calcium hydroxide in water with co-existence of gaseous CO_2 in ambient condition leads to the precipitation of sub-micrometric aggregates in the order of <1 μm. The size of the output aggregates strongly depends both on the precipitation condition (like mixing rate and initial concentration of the slurry) and the time of residing in the solution.

The DLS method showed almost monomodal distribution of the particles in the solution obtained by means of

the RDR. In the reactor, the stable, 30-nm-sized calcite nanocrystals are formed, and then they immediately agglomerate. The mean diameter of the aggregates decreases with the increasing mixing rate. However, at very high mixing rate (160 rpm), the mixing is not homogenous, which results in the smaller size of the agglomerates. The size of the aggregates is also dependent on the initial concentration of the slurry. Consequently, the higher the concentration of the slurry the larger the aggregates are formed.

The obtained results allow for the general conclusion concerning formation of nanoparticle in the RDR depending on process conditions. At low mixing rate, the high supersaturation degree occurs in the liquid film on disc's surface, and small crystallites can be formed. When discs rotate with higher rate, the liquid film is faster renewed; so, at a certain speed of the disc rotation (in the case of the reactor—160 rpm), the supersaturation degree is not achieved, which results in slightly larger-sized crystallites.

It is important to notice that the obtained particles have some impurities on their surface. They can be removed by heating them up to 400 °C in a laboratory oven for about 2 h. The heating leads to the obtainment of chemically pure aggregates of calcite which have the average size equal to about 950 nm.

A new, extended model for description of crystallization process taking place in the rotating disc reactor has been proposed. The internally consistent model very well describes both the formation and the aggregation of the calcite nanoparticles and can be used and recommended for accurate calculation of the particles' and aggregates' sizes as well as their distribution in the reactor.

The obtained results suggest that the carbonation of calcium hydroxide in the presence of gaseous CO_2 at ambient condition could be a powerful technique for producing fine sub-micrometric particles of calcite on an industrial scale.

Acknowledgements The research was partially supported by the European Union within European Regional Development Fund, through grant Innovative Economy (POIG.01.01.02-14-102/09).

References

1. Yue L, Shui M, Xu Z. The decomposition kinetics of nanocrystalline calcite. Thermochim Acta. 1999;335:121–6.
2. Spanos N, Koutsoukos PG. Kinetics of precipitation of calcium carbonate in alkaline pH at constant supersaturarion. spontaneous and seeded growth. J Phys Chem B. 1998;102:6679–84.
3. Rigopoulos S, Jones A. Modeling of semibatch agglomerative gas–liquid precipitation of CaCO(3) in a bubble column reactor. Ind Eng Chem Res. 2003;42:6567–75.
4. Schlomach J, Quarch K, Kind M. Investigation of precipitation of calcium carbonate at high supersaturations. Chem Eng Technol. 2006;29:215–20.
5. Sohnel O, Mullin JW. Precipitation of calcium carbonate. J Cryst Growth. 1982;60:239–50.
6. Reddy MM, Nancollas GH. Crystallization of calcium-carbonate. 4. Effect of magnesium, strontium and sulfate-ion. J Cryst Growth. 1976;35:33–8.
7. Kazmierczak TF, Tomson MB, Nancollas GH. Crystal growth of calcium carbonate. A controlled composition kinetic study. J Phys Chem. 1982;86:103–7.
8. Dindore VY, Brilman DWF, Versteeg GF. Hollow fiber membrane contactor as a gas–liquid model contactor. Chem Eng Sci. 2005;60:467–79.
9. Jung T, Kim WS, Choi CK. Effect of monovalent salts on morphology of calcium carbonate crystallized in Couette–Taylor reactor. Cryst Res Technol. 2005;40:586–92.
10. Kitano Y, Park K, Hood DW. Pure aragonite synthesis. J Geophys Res. 1962;67:4873–4.
11. Chen JF, Wang YH, Guo F, Wang XM, Zheng Ch. Synthesis of nanoparticles with novel technology: high-gravity reactive precipitation. Ind Eng Chem Res. 2000;39:948–54.
12. Cafiero LM, Baffi G, Chianese A, Chianese A, Jachuck RJJ. Process intensification: precipitation of barium sulfate using a spinning disk reactor. Ind Eng Chem Res. 2002;41:5240–6.
13. Feng B, Yonga AK, Ana H. Effect of various factors on the particle size of calcium carbonate formed in a precipitation process. Mater Sci Eng A. 2007;445–446(15):170–9.
14. Montes-Hernandez G, Renard F, Geoffroy N, Charlet L, Pironon J. Rhombohedral calcite precipitation from CO_2–H_2O–$CaOH)_2$ slurry under supercritical and gas CO_2 media. J Cryst Growth. 2007;308:228–36.
15. Judat B, Kind M. Morphology and internal structure of barium sulfate—derivation of a new growth mechanism. J Colloid Interface Sci. 2004;269:341–53.
16. Chakraborty D, Bhatia SK. Formation and aggregation of polymorphs in continuous precipitation. 2. Kinetics of CaCO3 precipitation. Ind Eng Chem Res. 1996;35:1995–2006.
17. Cheng B, Lei M, Yu JG, Zhao XJ. Preparation of monodispersed cubic calcium carbonate particles via precipitation reaction. Mater Lett. 2004;58:1565–70.
18. Meldum FC, Sear RP. Now you see them. Science. 2008;322:1802–3.
19. Colfen H, Antonietti M. Mesocrystals: inorganic superstructures made by highly parallel crystallization and controlled alignment. Angew Chem Int Ed. 2005;44:5576–91.
20. Dove PM, Hochella MF Jr. Calcite precipitation mechanisms and inhibition by orthophosphate: in situ observation by scanning force microscopy. Geochim Cosmochim Acta. 1993;57:705–14.
21. Paquette J, Reeder RJ. Relationship between surface structure, growth mechanism, and trace element incorporation in calcite. Geochim Cosmochim Acta. 1995;59:735–49.
22. Freij SJ, Putnis A, Astilleros JM. Nanoscale observations of the effect of cobalt on calcite growth and dissolution. J Cryst Growth. 2004;267:288–300.
23. Dalas E, Chalias A, Gatos D, Barlos K. The inhibition of calcium carbonate crystal growth by the cysteine-rich Mdm2 peptide. J Colloids Interface Sci. 2006;300:536–42.
24. Kędra-Królik K, Gierycz P. Obtaining calcium carbonate in a multiphase system by the use of new rotating disc precipitation reactor. J Therm Anal Calorim. 2006;83(3):579–82.

25. Kędra-Królik K, Gierycz P. Simulation of nucleation and growing of $CaCO_3$ nanoparticles obtained in the rotating disc reactor. J Cryst Growth. 2010;312:1945–51.
26. Carretti E, Chelazzi D, Rocchigiani G, Baglioni P, Poggi G, Dei L. Interactions between nanostructured calcium hydroxide and acrylate copolymers: implications in cultural heritage conservation. Langmuir. 2013;29(31):9881–90.
27. Natali I, Tempesti P, Carretti E, Potenza M, Sansoni S, Baglioni P, Dei L. Aragonite crystals grown on bones by reaction of CO2 with nanostructured Ca(OH)2 in the presence of collagen. Implications in archaeology and paleontology. Langmuir. 2014; 30(2):660–8.
28. Wang T, Antonietti M, Colfen H. Calcite mesocrystals: "morphing" crystals by a polyelectrolyte. Chem Eur J. 2006;12: 5722–30.
29. Elfil H, Roques H. Role of hydrate phases of calcium carbonate on the scaling phenomenon. Desalination. 2001;137:177–86.
30. Tlili MM, Amor MB, Gabrielli C, Joiret C, Maurin G, Rousseau P. Characterization of $CaCO_3$ hydrates by micro-Raman spectroscopy. J Raman Spectrosc. 2002;33:10–6.
31. Patterson A. The Scherrer formula for X-ray particle size determination. Phys Rev. 1939;56(10):978–82.
32. Klug HP, Alexander LE. X-ray diffraction procedures. New York: Wiley; 1974.
33. Hostomsky J, Jones AG. Calcium carbonate crystallization, agglomeration and form during continuous precipitation from solution. J Phys D. 1991;24:165–70.
34. Malkaj P, Chrissanthopoulos A, Dalas E. Understanding nucleation of calcium carbonate on gallium oxide using computer simulation. J Cryst Growth. 2004;264(1–3):430–7.
35. Halikia I, Zoumpoulakis L, Christodoulou E, Prattis D. Kinetic study of the thermal decomposition of calcium carbonate by isothermal methods of analysis. Eur J Miner Process Environ Prot. 2001;1(2):89–102.
36. Galan I, Glasser FP, Andrade C. Calcium carbonate decomposition. J Therm Anal Calorim. 2013;111:1197–202.
37. De Souza SPMC, De Morais FE, Dos Santos EV, Martinez-Huitle CA, Fernandes NS. Determination of calcium content in tablets for treatment of osteoporosis using thermogravimetry (TG). J Therm Anal Calorim. 2013;111:1965–70.
38. Forbes TZ, Radha AV, Navrotsky A. The energetics of nanophase calcite. Geochim Cosmochim Acta. 2011;75:7893–905.
39. Rodriguez-Navarro C, Ruiz-Agudo E, Luque A, Rodriguez-Navarro AB, Ortega-Huertas M. Thermal decomposition of calcite: mechanism of formation and textural evolution of CaO nanocrystals. Am Miner. 2009;94:578–84.
40. Wachi S, Jones AG. Mass transfer with chemical reaction and precipitation. Chem Eng Sci. 1991;46(4):1027–33.
41. Danckwerts PV. Gas–liquid reaction. New York: McGraw-Hill; 1970.
42. Randolph AD, Larson MA. Theory of particulate processes. 2nd ed. New York: Academic Press; 1988.
43. Bramley AS, Hounslow MJ, Ryall RL. Aggregation during precipitation from solution. A method for extracting rates from experimental data. J Colloids Interface Sci. 1996;183:155–65.
44. Hulburt HM, Katz S. Some problems in particle technology—statistical mechanical formulation. Chem Eng Sci. 1964;19: 555–74.
45. Collier AP, Hounslow MJ. A growth and aggregation rates for calcite and calcium oxalate monohydrate. IChE J. 1999;45: 2298–305.
46. Davies CW. Ion association. London: Butterworths; 1962.
47. Sutherland W. Dynamical theory of diffusion for non-electrolytes and the molecular mass of albumin. Philos Mag. 1905;9:781–5.
48. Nielsen AE. Kinetics of precipitation. Oxford: Pergamon Press; 1964.
49. Packter A. The precipitation of sparingly soluble alkaline-earth metal and lead salts: nucleation and growth orders during the induction period. J Chem Soc A. 1968;859–62.
50. Reddy MM, Nancollas GH. The crystallization of calcium carbonate. I. Isotopic exchange and kinetics. J Colloid Interface Sci. 1971;36:166–72.
51. Capuder E, Koloini T. Gas hold-up and interfacial area in aerated suspensions of small particles. Chem Eng Res Des. 1984;62: 255–60.
52. Plummer LN, Busenberg E. The solubilities of calcite, aragonite and vaterite in CO2–H2O solutions between 0 and 90 °C and an evaluation of the aqueous model for the system CaCO3–CO2–H2O. Geochim Cosmochim Acta. 1982;46:1011–40.
53. Astarita G. Mass transfer with chemical reaction. Amsterdam: Elsevier; 1967.
54. Maslen EN, Streltsov VA, Streltsova NR. X-ray study of the electron density in calcite, $CaCO_3$. Acta Cryst. 1993;B49:636–41.